Research Article Vol. 15, No. 9 / 1 Sep 2024 / *Biomedical Optics Express* 5199

Biomedical Optics EXPRESS

Comparison of vinculin tension in cellular monolayers and three-dimensional multicellular aggregates

LUNI HU,[1] RICK I. COHEN,[1] MARGARIDA BARROSO,[2] AND NADA N. BOUSTANY[1,*]

[1] *Department of Biomedical Engineering, Rutgers University, Piscataway, NJ 08854, USA*
[2] *Department of Molecular and Cellular Physiology, Albany Medical College, Albany, NY 12208, USA*
[*] *nboustan@rutgers.edu*

Abstract: Confocal frequency-domain fluorescence lifetime and Förster resonance energy transfer (FRET) microscopy of Chinese hamster ovary (CHO-K1) cells expressing the vinculin tension sensor (VinTS) is used to compare vinculin tension in three-dimensional (3D) multicellular aggregates and 2D cellular monolayers. In both 2D and 3D cultures, the FRET efficiency of VinTS is 5-6% lower than that of VinTL ($p < 0.05$), a tail-less control which cannot bind actin or paxillin. The difference between VinTS and VinTL FRET efficiency can be mitigated by treatment with the Rho-associated kinase inhibitor Y-27632, demonstrating that VinTS is under tension in both 2D and 3D cultures. However, there is an overall decrease in FRET efficiency of both VinTS and VinTL in the 3D multicellular aggregates compared with the 2D monolayers. Expression of VinTS in 2D and 3D cultures exhibits puncta consistent with cellular adhesions. While paxillin is present at the sites of VinTS expression in the 2D monolayers, it is generally absent from VinTS puncta in the 3D aggregates. The results suggest that VinTS experiences a modified environment in 3D aggregates compared with 2D monolayers and provide a basis for further investigation of molecular tension sensors in 3D tissue models.

1. Introduction

Mechanical forces and the cytoskeleton play a significant and central role in shaping cellular function and behavior. Mechanotransduction, imparted though cell-extracellular matrix (ECM) and cell-cell interactions, has been implicated in the behavior of cells participating in different processes, including embryonic development, angiogenesis, cancer cell metastasis, and neuronal growth [1–6]. The potential to control complex cellular functions via mechanotransduction has important implications for the design of therapeutic strategies to address pathological conditions, including degenerative diseases, tissue injury and repair, or cancer, in which tissue mechanics play a role.

In this context, 3-dimensional (3D) cultures constitute important models for investigating the role of cell-ECM and cell-cell adhesions in the regulation of cytoskeletal assembly and cellular behaviors such as attachment, proliferation, and migration, relevant to tissue growth [7,8]. To investigate neoplastic progression, multicellular cancer cell aggregates have been used extensively for several decades as avascular models of tumor spheroids [9–11]. Their ability to replicate the structure and biochemical gradients in *in vivo* tumors has made these aggregates relevant in the study of tumor growth, metastasis, and response to chemotherapeutic agents [12–15]. The influence of tissue mechanics on cellular behaviors within multicellular aggregates can be studied on different scales [16]. For example, mechanical pressure applied at the level of the whole multicellular spheroid affects cell motility, proliferation, dormancy and apoptosis [17–20] while hydrostatic pressure and fluid flow modulate cell migration of epithelial cells out of an aggregate embedded in a collagen matrix [21]. At the cellular level, methods to probe tension imparted by

#529156 https://doi.org/10.1364/BOE.529156
Journal © 2024 Received 20 May 2024; revised 31 Jul 2024; accepted 1 Aug 2024; published 13 Aug 2024

the cells within multicellular aggregates include a variety of approaches such as measuring the compression of spheres made of fluorescently labeled hydrogels, which are embedded within 3D multicellular aggregates [22], culturing multicellular aggregates surrounded by elastomeric pillars whose mechanical deformation can be quantified [23], or by inducing the growth of multicellular aggregates around gelatin fibers whose deformation is subsequently measured to infer mechanical stresses imparted on them by the surrounding cells [24]. Mechanical forces and displacements can also be evaluated at the molecular scale and here, we use molecular tension reporters [25] to measure molecular tension at adhesion sites within 3D multicellular aggregates. One advantage of these intracellular molecular tension probes is that they can ultimately be used to link the tension experienced by a specific load-bearing protein, such as vinculin, to the subsequent subcellular events leading to changes in cytoskeletal assembly and growth dynamics. Thus, one can elucidate the role of mechanical tension on proteins acting within a specific molecular pathway.

Molecular tension sensors are genetically constructed and typically comprise two fluorophores, acting as a Förster resonance energy transfer (FRET) donor-acceptor pair connected by a mechanosensing linker. Tension measurements rely on the principle of FRET, where upon excitation, energy is non-radiatively transferred from the donor to the acceptor when they are in close proximity, on the order of 10 nm. Extension of the linker under mechanical tension decreases FRET efficiency as the separation between the donor and acceptor increases and can be quantified by live cell fluorescence microscopy. Consequently, inserting the sensor into a protein of interest allows the detection of mechanical forces acting on that protein during a specific cellular process. One of the first tension sensors, designated stFRET and relying on FRET between mCerulean and mVenus, was integrated into α-actinin, filamin and spectrin [26]. Another, is the tension sensing module, TSMod, which was calibrated in single molecule force experiments and shown to have pico-Newton sensitivity [25]. TSMod was initially used to create the vinculin tension sensor (VinTS) to investigate the mechanical behavior of vinculin [25] and was subsequently inserted in several other proteins acting at cell-ECM and cell-cell adhesions, including E-cadherin [27], PECAM [28], α-catenin [29] and talin [30]. TSMod was utilized to probe forces at focal adhesions between the cell and extracellular matrix [31]. TSMod was also used in conjunction with nanobodies to construct a lamin tension sensor to study tension within the nuclear lamina located below the inner nuclear membrane [32]. Currently, FRET tension probes are being extensively employed in the investigation of cell mechanics across numerous studies and have been the subject of multiple reviews [33,34].

In this paper, we extend our previous fluorescence lifetime (FLIM) measurements [35] of VinTS made in two-dimensional (2D) cellular monolayers to three-dimensional (3D) multicellular aggregates. Our goal is to demonstrate the feasibility of utilizing VinTS in 3D aggregates in conjunction with our frequency-domain FLIM system and to compare directly and side-by-side, vinculin tension in 3D vs. 2D cultures generated from the same cell line. This study, conducted using Chinese Hamster Ovary (CHO-K1) cells, provides a baseline for future studies using human cancer cells. The results demonstrate that VinTS expressed in the 3D aggregates localizes to punctate structures consistent with adhesion sites. In both 2D and 3D cultures, the lifetime of VinTS was higher than the lifetime of the tail-less vinculin control probe (VinTL) unable to bind actin or paxillin. Treatment with the Rho-associated kinase inhibitor, Y-27632, decreased the lifetime of VinTS, while VinTL's lifetime remained unchanged, demonstrating an actin-myosin force-dependent behavior of VinTS lifetime at adhesion sites. However, an overall longer lifetime (lower FRET efficiency) was observed in the 3D aggregates for both VinTS and the VinTL control compared with the 2D cell monolayers. This result, along with the lack of spatial colocalization between VinTS and paxillin within the 3D multicellular aggregates, suggest that the 3D culture environment and potentially the formation of different types of adhesions, influences the FRET efficiency measurements within the 3D cultures.

2. Materials and methods

2.1. Tissue culture and transfection

Monolayers and 3D multicellular aggregates of CHO-K1 cells (ATCC CCL-61) were maintained at 37 °C in a 5% CO_2 in air atmosphere in Complete Growth Medium consisting of F12 K medium (ATCC 30-2004) supplemented with 10% fetal bovine serum (GeminiBio, Benchmark FBS 100-106). To avoid cell alterations due to continued cell culture passaging, all the cells used in the experiments were passaged less than 30 times. A passage corresponds to subculture of the cells wherein the current cells are subdivided into a new culture. While the experiments spanned multiple passages, the passage number of the control and experimental groups within each experimental run was matched. In the case of the multicellular aggregates, the cells were counted during passaging, and seeded at 18,000 cells per well, by seeding 200µL of a 90,000 cells/mL cell suspension in individual U-shaped wells of a low-attachment 96-well plate (Thermo-Fisher, Nunclon Sphera- Treated 96 well microplate). The cells proliferated and formed multicellular aggregates over the course of 2-5 days. On day 4 of the culture, the spheroids were transfected with plasmids encoding VinTS, VinTL, mTFP1, or TSMod. Plasmid sources are listed in Table 1. The tension sensor module (TSMod) comprises two fluorescent proteins, mTFP1 and mVenus, connected by an elastic linker. In VinTS, TSMod is inserted between the head and tail of Vinculin while VinTL lacks the vinculin tail preventing its binding to F-actin and paxillin [25]. VinTS transmits force-induced signals through the interaction of its head domain with the talin-integrin complex and its tail domain with the actin cytoskeleton. However, a tail-less vinculin construct (VinTL) can be recruited to focal adhesions (FA) by combining its head domain with the talin-integrin complex but cannot transmit force due to the lack of the F-actin binding domain. Therefore, in tension measurements, force-free VinTL can serve as a control compared to force-transmitting VinTS. VinTL's FRET efficiency provides a baseline measurement of the unloaded tension module expressed in vinculin in the environment within the adhesions, while the difference between the FRET efficiency of VinTS and VinTL reports on the level of tension present across vinculin. Transient transfection was achieved with Lipofectamine LTX with PLUS Reagent (Invitrogen). For each well containing a 3D multicellular aggregate, the transfection mix comprised 200µL of serum-free OPTIMEM (Invitrogen), 1.25 µg of DNA, 1.25 µL of PLUS reagent and 3 µL of Lipofectamine LTX. After removal of the growth medium, the multicellular aggregates were incubated with the transfection mix for 5 hours, after which the medium was switched back to Complete Growth Medium. For 2D monolayers, 50,000 cells were seeded in 3.5 cm culture dishes (9.62 cm^2) for a seeding density of ~5,000 cells/cm^2. On the next day, cells were transfected with 2.5 µg of DNA, 2.5 µL PLUS reagent and 6 µL of Lipofectamine LTX (per dish) for 1.5 hours in 2 mL serum-free OPTIMEM medium (Invitrogen). After 1.5 hours, the medium was switched back to Complete Growth Medium. For the immunofluorescence studies, CHO-K1 monolayers were plated on 12 mm flame-sterilized glass coverslips (12-545-81, Fisher scientific) coated with 1 mL of 10 µg/mL poly-D-lysine (P0899, Sigma-Aldrich) diluted in sterile water.

Table 1. Plasmid description and origin

Plasmid	Origin	Addgene	Web address	RRID
VinculinTS (VinTS)	M. Schwartz [25]	# 26019	http://n2 t.net/addgene:26019	26019
Tail-less VinculinTS (VinTL)	M. Schwartz [25]	# 26020	http://n2 t.net/addgene:26020	26020
TS module (TSMod)	M. Schwartz[25]	# 26021	http://n2 t.net/addgene:26021	26021
mTFP1	B.D. Hoffman (Duke University)	NA	NA	NA

2.2. Fluorescence lifetime imaging

Live cell imaging of the multicellular aggregates was performed on day 3 after transfection. Prior to imaging, the aggregates were transferred to a glass coverslip and embedded in 1.25% low-melt agarose (Sigma A9045), which was gelled in Imaging Medium (Leibowitz L15 medium (Invitrogen) + 10% fetal bovine serum + 1% penicillin/ streptomycin). The agarose-embedded aggregates were immersed in imaging medium and imaged using frequency-domain fluorescence lifetime imaging microscopy (FLIM), as previously described by Dumas et al. [35]. Two channels encoding the fluorescence intensity and phase lifetime of mTFP1 are collected simultaneously. The excitation wavelength is 450 nm, and the emission bandwidth is centered at 479 (+/-20) nm. The 450 nm excitation laser was sinusoidally modulated at 42.1875MHz and had a power of 19-22µW at the sample. A solution consisting of 0.1 mM coumarin 6 (Sigma-Aldrich # 546283) in ethanol (0.6 mg dissolved in 20 mL of ethanol) with known lifetime of 2.5 ns was used to calibrate the lifetime measurement as previously described [35]. In this study, a 60x water dipping objective with NA 1.0 (Nikon, CFI APO 60X W NIR, MRD07620) was used. Our FLIM system is an upright microscope and this high NA water dipping objective was chosen due to its long working distance (2.8 mm). This upright setup was chosen to allow us to focus on the surface of thick samples from various distances without being affected by the thickness of the coverslip, as can occur with inverted microscopy. The NA of the objective allowed for resolving individual focal adhesions. The 2D cellular monolayers were imaged in the 3.5 cm culture dish in Imaging Medium using the same water immersion objective on day 2 after transfection. In the case of the multicellular aggregates expressing VinTS, or VinTL, z-stacks consisting of 16 sections (VinTS) or 11 sections (VinTL) with 2µm steps were acquired; for aggregates expressing mTFP1 or TSMod, z-stacks consisted of 21 sections (mTFP1) or 13 sections (TSMod) with 5um steps. All images were captured at 1024 × 1024 scanned points with a dwell time of 6.8µs per point (7.1s per frame).

2.3. Image analysis and calculation of FRET efficiency

The images of samples expressing VinTS or VinTL were analyzed by creating a binary mask to segment the adhesion puncta followed by calculating the intensity-weighted mean lifetime within these regions of interest. In the case of the image stacks acquired from the multicellular spheroids, each section was analyzed individually. Initial image segmentation was performed using the open-source ImageJ Fiji software [36] following the approach taken by Dubois et al [37]. First, a rolling ball background subtraction (ball radius = 30 pixels) was applied to the intensity image. Next, a Gaussian blur (σ = 2 pixels) was applied to smooth the outline of the regions of interest (ROIs). A binary mask was obtained by manually defining a threshold value to separate the adhesions from the background. This threshold varied depending on the intensity of the original image. A segmented lifetime image of the adhesions was generated by multiplying the binary mask with the original lifetime image. The details are shown in Supplement 1. The intensity-weighted mean lifetime within each segmented ROI was calculated using MATLAB (MathWorks, Inc.) and assigned to the corresponding ROIs (Sup. Fig. S1i). The intensity-weighted mean lifetime was calculated using the following formula:

$$\bar{\tau}_w = \frac{\sum_{i=1}^{n} \tau_i \times I_i}{\sum_{i=1}^{n} I_i} \tag{1}$$

I_i is the intensity value at each pixel, τ_i is the corresponding lifetime value at each pixel, and n is the number of pixels in the ROI. Pixels with relative intensity value less than 0.01(less than 10% of maximum) or lifetime value above 5 ns are excluded from analysis. A similar approach was used to analyze the images of cells expressing mTFP1 or TSMod. In this case, the cells were segmented using a manual threshold and the intensity-weighted mean lifetime was calculated on a per-cell basis.

The intensity-weighted phase lifetime measured by the FD-FLIM system was converted to an Apparent FRET efficiency (E_{App}) for each ROI:

$$E_{App} = 1 - \frac{\bar{\tau}_w}{\tau_D} \tag{2}$$

$\bar{\tau}_w$ is the measured intensity-weighted mean lifetime (Eq. 1), τ_D is the established lifetime of the donor, mTFP1, without an acceptor. We set the value of τ_D= 3.11 ns, based on a previous fit of phase data performed at multiple modulation frequencies [38]. We had shown that the apparent FRET efficiency is linearly related to True FRET efficiency in the frequency range between 14 and 56 MHz [38]. Thus, at the modulation of 42.2 MHz used in this study, we expect:

$$E_{App} = m \cdot E_{True} + b \tag{3}$$

The slope, m, and intercept, b, were determined in this study by measuring the phase lifetime and apparent FRET efficiency of mTFP1 and TSMod corresponding to a true FRET efficiency of 0 for mTFP1 and 0.279 for TSMod in CHO-K1 cells [37], respectively. A non-zero intercept corresponds to $b = \left(1 - \frac{\tau_\phi^{TFP}}{\tau_D}\right)$ where τ_ϕ^{TFP} is the measured phase lifetime of mTFP1 that may differ slightly from τ_D= 3.11 ns at a given frequency. The apparent FRET efficiency calculated from the measured phase lifetime of VinTS and VinTL can therefore be converted to true FRET efficiency using Eq. 3 after determining the slope and intercept. A decrease in lifetime corresponds to an increase in FRET efficiency.

2.4. Treatment with Y27632

The 5 mM stock solution of Y-27632 (688001, Sigma-Aldrich) was diluted to a final concentration of 10 µM in serum-free F12 K medium, which was used to treat the samples. Cells and multicellular aggregates expressing VinTS or VinTL were treated with 10 µM Y-27632 or vehicle (4 µL sterile water in 2 mL serum-free F12 K medium) for 2 hours (2D cultures) or between 2 and 2.5 hours (3D cultures) at 37°C and 5% CO2. The drug treatment time was extended to allow for penetration of the reagent into the 3D aggregates. After incubation, the medium was switched to Imaging Medium, and the treated samples were imaged as described in Section 2.2 above.

2.5. Immunofluorescence

2D cell monolayers and 3D multicellular aggregates were rinsed 1x with phosphate buffered saline (PBS) (Gibco, 10010), and then fixed with 4% paraformaldehyde (PFA) for 15 min at room temperature. The 4% PFA solution was prepared by dissolving 4 g of PFA powder (Sigma-Aldrich, P6148) in 100 mL of PBS and then heating the solution to 60°C while stirring continuously until it turns clear. After fixation, samples were washed 3x with PBS with 10- minute intervals between washes. The samples were permeabilized with 0.3% Triton X-100 (Sigma-Aldrich, 93443) in PBS for 15 min at room temperature followed by 3x PBS washes. The samples were incubated with blocking solution consisting of 5% bovine serum albumin (BSA) in PBS, for an hour at room temperature to prevent non-specific binding. After blocking, samples were incubated with primary antibodies diluted in blocking solution overnight at 4°C. The samples were then washed 3x 10 min with PBS and incubated with secondary antibody diluted in blocking solution for 1 hour at room temperature. Samples were rinsed in PBS and incubated with 2 µg/mL Hoechst 33342 (Thermo-Fisher, Molecular Probes, H-21492) for 15 minutes to stain nuclei. Following a 1x rinse with PBS, the multicellular aggregates were transferred to glass bottom slides (Ibidi, 80807) for imaging. The stained coverslips (2D monolayers) were mounted on a glass slide with Fluoromount solution (Thermo-Fisher, 00-4958-02) and were allowed to dry overnight before imaging. Primary antibodies include mouse monoclonal anti-vinculin (Thermo-Fisher) and mouse monoclonal anti-paxillin (Thermo-Fisher). Secondary antibodies include AlexaFluor 488 goat-anti-mouse (Invitrogen), and AlexaFluor 647 goat-anti-mouse (Invitrogen). Table 2 lists the primary and secondary antibody sources and concentrations used in this experiment. Fluorescence imaging of the immunostained samples was conducted using confocal microscopy (Zeiss 780 LSM) independently of the FLIM system. The excitation and emission settings for immunofluorescence are listed in Table 3. The cross-talk between the Alexa 488 and 647 channels was negligible (Supplement 1).

Table 2. Antibody source and concentration

Antibody	Primary/ secondary	Stock concentration	Dilution	Host	Published Target Species	Source
Anti-Vinculin	Primary	1 mg/mL	1:200	Mouse	Hamster	Millipore-Sigma: SAB4200729
Anti- Paxillin	Primary	5.9 mg/mL	1:250	Mouse	Hamster	Thermo-Fisher: MA1-24952
Alexafluor-488	Secondary	2 mg/mL	1:1000	Goat	Mouse	Invitrogen: A28175
Alexafluor-647	Secondary	2 mg/mL	1:1000	Goat	Mouse	Invitrogen: A21236

Table 3. Laser settings in the immunofluorescence study

Dye	Excitation	Emission
Hoechst	405nm	415-450nm
Alexa Fluor 488	488nm	498-535nm
Alexa Fluor 647	633nm	652-693nm

3. Results

3.1. Expression of VinTS in 2D and 3D cultures

VinTS expression was localized to punctate structures in CHO-K1 cells cultured in monolayers and in 3D multicellular aggregates (Fig. 1). In cultured 2D monolayers, the fluorescent puncta displayed a similar morphology to that of focal adhesions in adherent cells [25]. VinTS expression in the multicellular aggregates was limited to the periphery of the spheroid (Fig. 2) with the fluorescent region on the periphery accounting for 20-30% of the entire spheroid. Within the peripheral region of the aggregates, the transfection efficiency was 4-15% (based on the fluorescent images collected) compared to >50% in the 2D monolayers. In optical sections imaged at high magnification, the puncta's appearance in the 3D multicellular aggregates appeared sparser and less elongated compared with the focal adhesions of 2D monolayers. To confirm the presence of vinculin at the observed puncta, the transfected samples were immunostained with anti-vinculin antibody. Observations were made in N = 35 cells from 2 experimental repeats in 2D monolayers, and N = 30 cells from 3 experimental repeats in multicellular aggregates). As seen in Fig. 1, vinculin immunostaining (red) co-localized with VinTS (green) expressed in the transfected cells, and also labeled endogenous vinculin in the surrounding untransfected cells (dotted yellow boxes in Figs. 1(a) and 1(e)). In both 2D and 3D culture environments, the morphology and distribution of VinTS puncta were similar to those of endogenous vinculin in the untransfected cells. Some cells in the 3D multicellular aggregates expressed VinTS but were not labeled with anti- vinculin antibody (white arrow in Fig. 1(e)) likely due to less uniform antibody labeling in the 3D aggregate compared with the 2D monolayers.

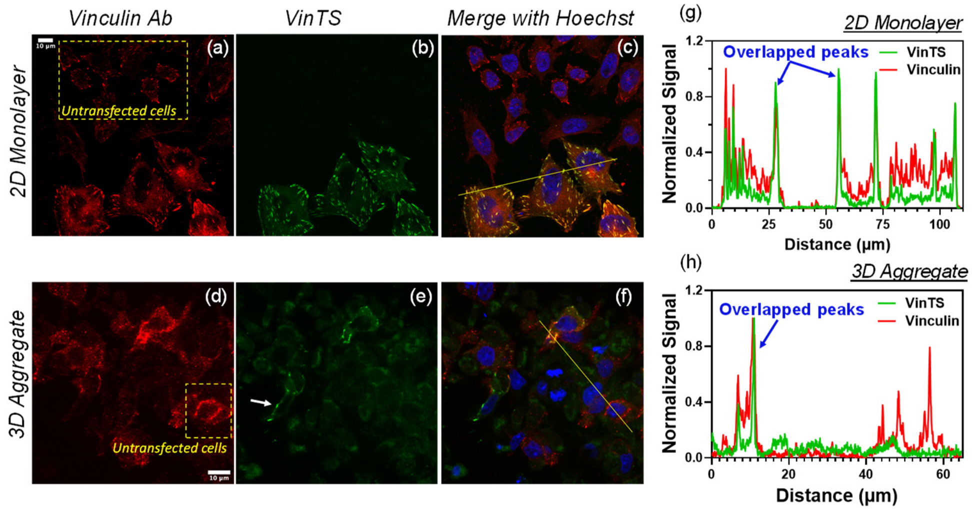

Fig. 1. CHO-K1 cells expressing VinTS alongside untransfected cells (dotted yellow boxes) were immunostained with vinculin primary antibody labeled with Alexa-647-conjugated secondary antibody in a 2D monolayer (top panels) and a 3D multicellular aggregate (bottom panels). (a, d) Alexa-647 fluorescence (red pseudocolor). (b, e) VinTS fluorescence (green pseudocolor). The white arrow in (e) indicates a region with VinTS expression but no antibody staining likely due to less uniform antibody labeling in the 3D aggregate compared with the 2D monolayers. (c, f) Merged images including Hoechst staining of the nuclei (blue pseudocolor). (g) and (h) Signal cross sections along the lines in the merged images (c and f) show overlapping peaks in the Alexa-647 and VinTS channels at sites of VinTS expression.

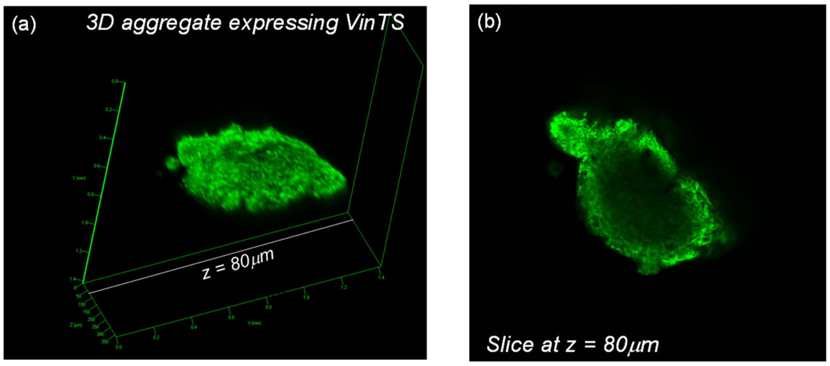

Fig. 2. CHO-K1 multicellular aggregate expressing VinTS observed by confocal microscopy at low magnification. (a) Volume reconstruction, (b) Slice at z = 80 μm showing VinTS expression primarily at the periphery of the aggregate.

3.2. VinTS is under tension in 2D and 3D cultures

Donor (mTFP1) intensity and lifetime images of cells expressing VinTS or VinTL are shown in Fig. 3 for the 2D monolayers and 3D aggregates. 3D volume rendering of the multicellular aggregates is presented in Supplement 1. In both culture environments, VinTS exhibited longer lifetime values and expanded lifetime range compared with VinTL (Fig. 3(d), 3(e)). In 2D cultures, the intensity-weighted mean lifetime at focal adhesion sites is 2.18 ns +/- 0.113 ns for VinTL (N = 4806 adhesions from 4 experimental repeats) and 2.31 ns +/- 0.13 ns for VinTS (N = 5268 adhesions from 4 experimental repeats) (Fig. 3(d)). The difference is statistically significant ($p < 0.0001$). In 3D multicellular aggregates, the lifetime of VinTL at putative adhesions is 2.34 ns +/- 0.121 ns (N = 1889 adhesions from 3 experimental repeats) compared with 2.50 ns +/- 0.149 ns (N = 1186 adhesions from 3 experimental repeats) for VinTS ($p < 0.0001$) (Figure 3(e)).

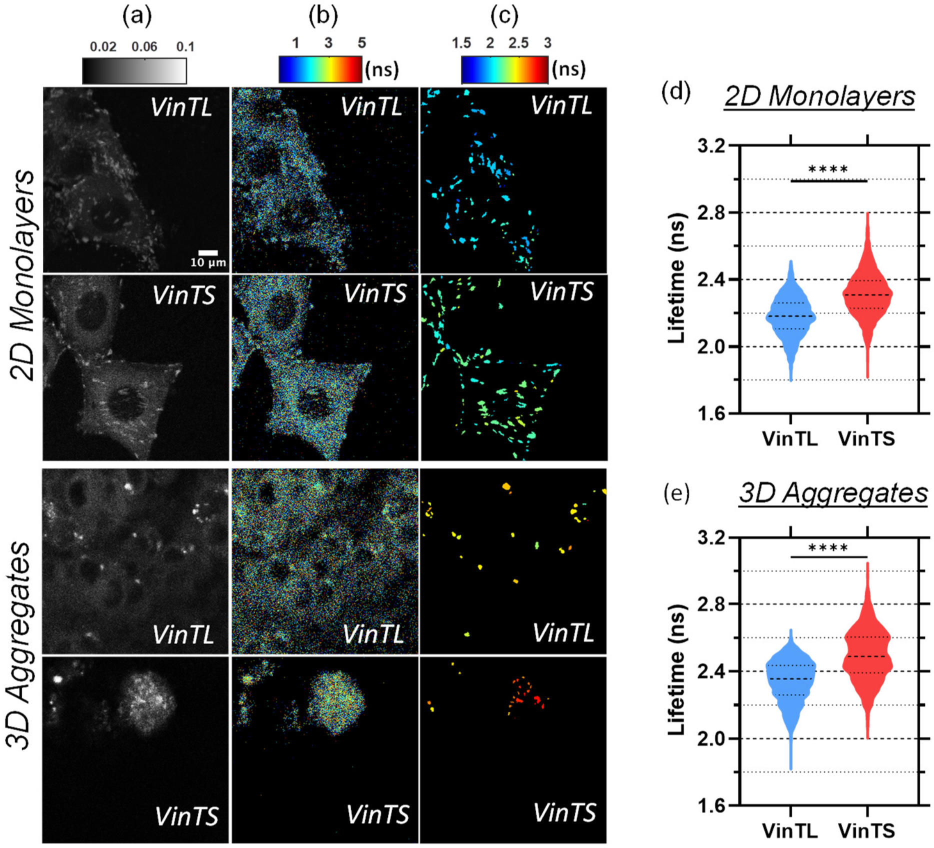

Fig. 3. Representative images of CHO-K1 cells expressing VinTS or VinTL in 2D monolayers (top panels) and in an optical section of a multicellular aggregate (bottom panels). (a) Donor intensity, (b) corresponding fluorescence lifetime, and (c) processed lifetime images after assigning the intensity-weighted mean lifetime value to each segmented adhesion region. A 3D volume rendering of the multicellular aggregates is presented in Supplement 1. (d) and (e) Violin plots of the intensity-weighted mean lifetime of all adhesions analyzed in the 2D monolayer cultures (d) and the multicellular aggregates (e). The lifetime of VinTS is significantly longer than that of VinTL (**** denotes $p < 0.0001$ by Mann-Whitney test).

To demonstrate that the measured lifetime difference between VinTS and VinTL is force dependent, samples expressing VinTL and VinTS were treated with 10 µM Y-27632. Y-27632 inhibits actin-myosin contractility by inhibiting Rho-associated protein kinase (ROCK). After treatment, the lifetime of VinTS was significantly decreased from 2.3 to 2.2 ns ($p < 0.05$, N = 3 experimental repeats) in the 2D cultures, while the lifetime of VinTL remained unchanged (Fig. 4(a)). Treatment of the 3D multicellular aggregates with Y-27632 resulted in reducing the lifetime of VinTS from 2.45 ns to 2.34 ns ($p < 0.05$, N = 3 experimental repeats), while the VinTL lifetime remained unchanged (Fig. 4(b)). The observed decrease in the lifetime of VinTS in response to myosin inhibition indicates that VinTS is under tension in 2D monolayer cultures as well as within the 3D multicellular aggregates.

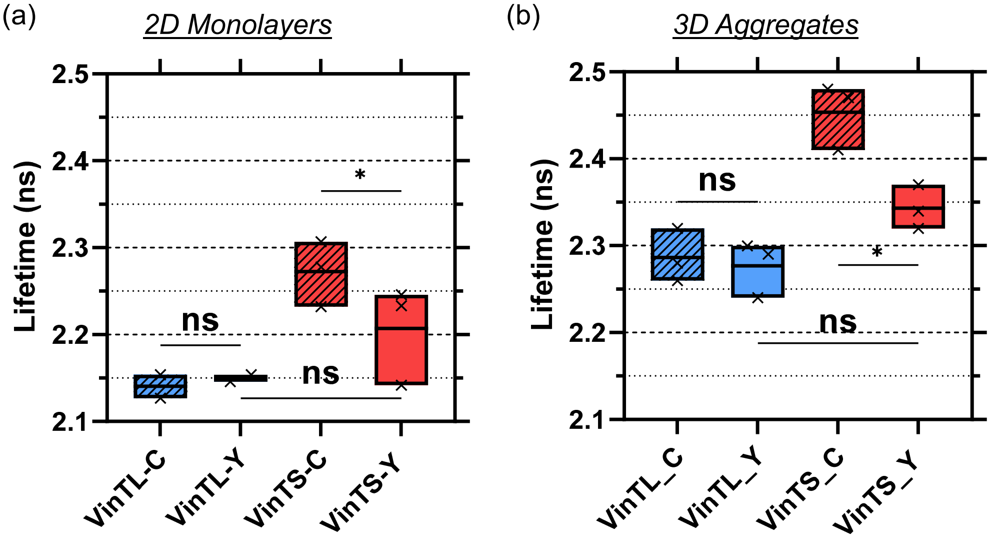

Fig. 4. VinTS and VinTL lifetime in (a) 2D monolayers and (b) 3D multicellular aggregates after treatment with the Rho-associated kinase inhibitor Y-27632. VinTS-C and VinTL-C are controls treated with sterile water, VinTS-Y and VinTL-Y are treated with 10μM Y-27632. * $p < 0.05$ (ANOVA with repeated measured followed by Fisher's Least Significance Difference post-hoc test). Each point within the box plot represents a separate experiment. The boxes length extends from the minimum to the maximum value and the line denotes the mean. Results of multi-comparisons statistics tests may be found in Supplement 1.

3.3. *FRET efficiency of VinTS and VinTL in 2D and 3D cultures*

To convert the measured phase lifetime to FRET efficiency, the FD-FLIM system was used to measure the fluorescence lifetime of mTFP1 and TSMod and determine the slope and intercept of Eq. 3 (Methods) (Fig. 5(a-c)). The average lifetime of mTFP1 was 2.86 ns +/- 0.036 ns (N = 55 cells) in CHO-K1 monolayers and 2.84 ns +/- 0.086 ns (N = 67 cells) in multicellular aggregates, respectively. Meanwhile, the measured average lifetime of TSMod was 2.25 ns +/- 0.074 ns (N = 79 cells) in the monolayers and 2.11 ns +/- 0.11 ns (N = 76 cells) in the multicellular aggregates. The significant difference in the fluorescence lifetime of TSMod between 2D monolayers and 3D multicellular aggregates is likely due to photobleaching of the acceptor (mVenus) in the case of the 2D monolayers as explained in Supplement 1. However, photobleaching tests on VinTL showed that the lifetime of VinTL in the 2D monolayers was not affected by acceptor photobleaching (Supplement 1). Thus, we used the lifetime of mTFP1 and the unbleached lifetime of TSMod taken from the 3D culture data in Fig. 5(c) to obtain a two-point calibration (Supplement 1) with:

$$E_{App} = 0.8452 \cdot E_{True} + 0.08676 \tag{4}$$

Equations 2 and 4 were applied to both 2D and 3D culture samples to convert the measured phase lifetime of VinTL and VinTS to True FRET efficiency (Fig. 5(d)).

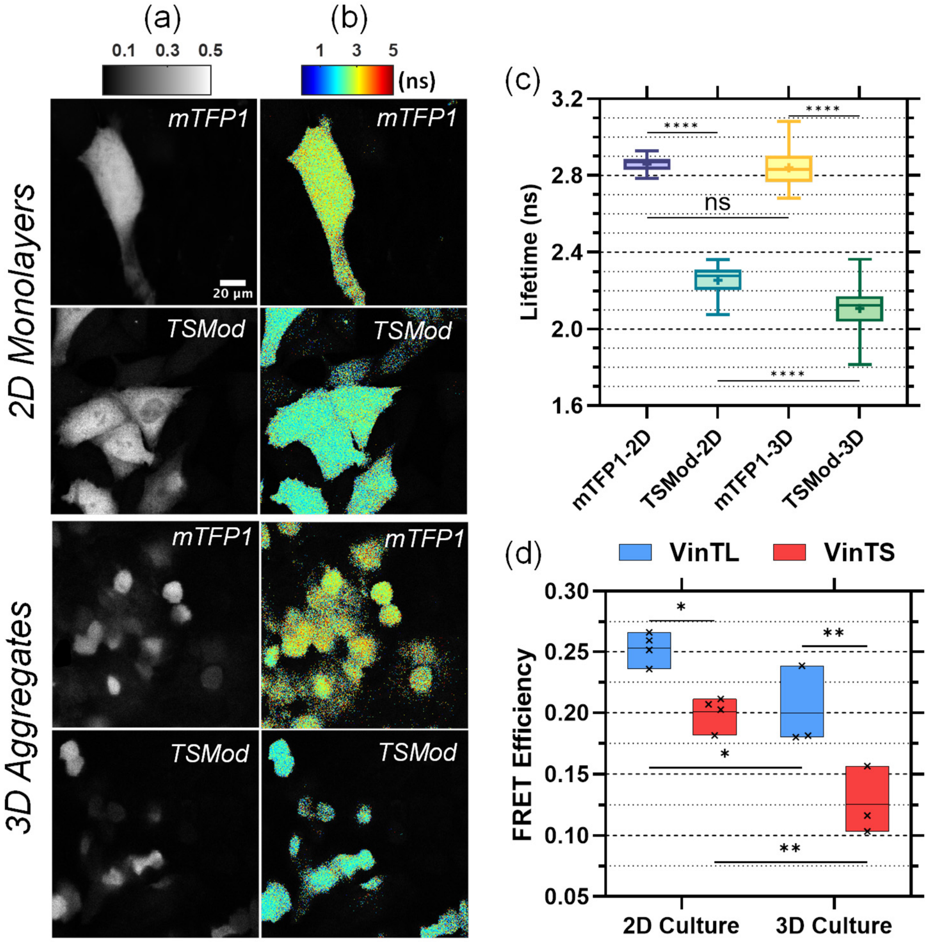

Fig. 5. Conversion of measured lifetime to FRET efficiency based on mTFP1 and TSMod. Representative donor intensity (a) and lifetime (b) images of mTFP1 and TSMod in 2D monolayers (top panels) and multicellular aggregates (bottom panels). (c) Analysis of intensity-weighted mean lifetime per cell for all mTFP1 and TSMod data. **** denotes $p < 0.0001$, 'ns' (not significant) denotes $p > 0.05$ (One-way ANOVA followed by Dunn's post hoc multiple comparisons tests). The boxes length is the interquartile range (IQR) extending from the 25^{th} to th 75^{th} percentile, the line denotes the median, the point the mean, and the whiskers extend to the minimum and maximum value. (d) FRET efficiency of VinTS and VinTL after conversion of the measured phase lifetime to True FRET efficiency (Eqs. 2-4). Each point within the box plot represents a separate experiment. The boxes length extends from the minimum to the maximum value and the line denotes the mean. * denotes $p < 0.05$; ** $p < 0.01$ (Two-way ANOVA followed by Tukey's post hoc multiple comparisons test). Results of multi-comparisons statistics tests may be found in Supplement 1.

The calculated FRET efficiency of VinTL was 25.07% +/- 4.31% and of VinTS 20.07% +/- 4.92% in 2D monolayers, while the FRET efficiency of VinTL and VinTS were 18.99% +/- 4.6% and 13.12% +/- 5.66%, respectively, in 3D multicellular aggregates (Fig. 5(d)). A summary of the lifetime and FRET efficiency values is included in Table 4.

In both 2D monolayers and 3D multicellular aggregates, the difference between VinTS and VinTL was statistically significant ($p < 0.01$). A two-way ANOVA resulted in a p-value of 0.36

Table 4. Summary of Lifetime and FRET efficiency values

Culture	Construct	Lifetime(ns)	FRET Efficiency (%)
2D monolayers	VinTL	2.18 +/- 0.113	25.07 +/- 4.31
	VinTS	2.31 +/- 0.130	20.07 +/- 4.92
3D aggregates	VinTL	2.34 +/- 0.121	18.99 +/- 4.60
	VinTS	2.50 +/- 0.149	13.12 +/- 5.66

for the interaction between plasmid (VinTS/VinTL) and culture environment (2D monolayers/ 3D cultures), suggesting that the FRET efficiency difference between VinTS and VinTL was not significantly affected by the culture environment. However, the results show that the FRET efficiency of both VinTL and VinTS was significantly lower in the 3D multicellular aggregates compared with the 2D monolayers (Table 5 $p < 0.001$ for culture method). To investigate if this difference is due to a difference in the environment of cell adhesions in 2D and 3D cultures, we used immunofluorescence to compare the presence of paxillin at the VinTS expression sites. The co-staining results indicate that paxillin is present at the VinTS sites in the 2D monolayers ($N = 52$ cells observed in 2 experimental repeats). However, while paxillin was present throughout the 3D multicellular aggregates, VinTS was not typically localized with paxillin ($N = 12$ cells observed in 2 experimental repeats). An example is shown in Fig. 6. In particular, the cell in which VinTS is expressed contains paxillin but the paxillin signal peaks are spatially distinct from the VinTS fluorescence signal peaks. In the cells observed, there were only three individual adhesions where VinTS and paxillin overlapped, each located within a different cell.

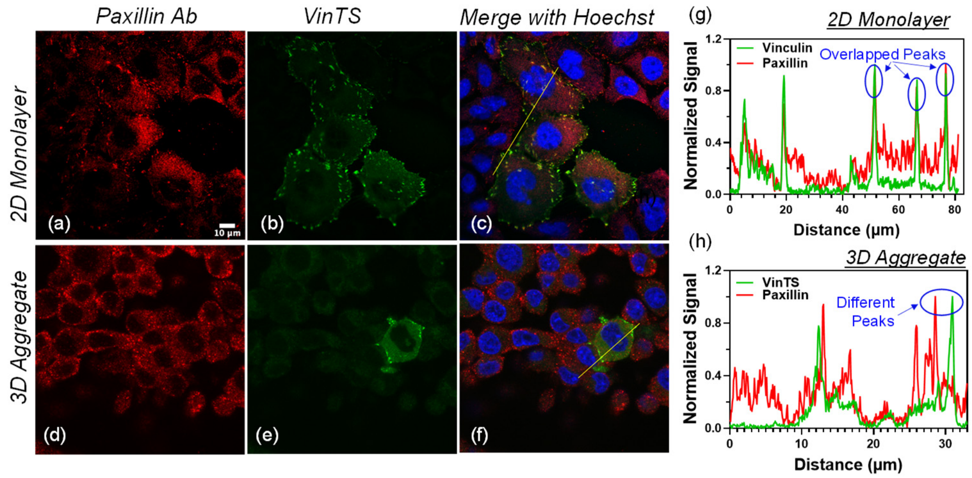

Fig. 6. CHO-K1 cells expressing VinTS and immunostained with paxillin primary antibody labeled with Alexa-647-conjugated secondary antibody in a 2D monolayer (top panels) and a 3D multicellular aggregate (bottom panels). (a, d) Alexa-647 fluorescence (red pseudocolor), (b, e) VinTS fluorescence (green pseudocolor). (c, f) Merged images including Hoechst staining of the nuclei (blue pseudocolor). (g) and (h) Signal cross sections along the lines in the merged images (c and f) show overlapping peaks in the Alexa-647 and VinTS channels at sites of VinTS expression in the 2D monoloayer but separate peaks in the 3D multicellular aggregate.

Table 5. Descriptive statistics of the two-way ANOVA test (Fig. 5(d) data)

Source of Variation	P value	P value summary
Interaction (method.plasmid)	0.3638	not significant (ns)
Culture method (2D/3D)	0.0003	***
Plasmid (VinTS/VinTL)	0.0003	***

4. Discussion

We investigated the vinculin tension sensor, VinTS, in 2D monolayers and 3D multicellular aggregates using fluorescence lifetime microscopy. In both types of cultures, VinTS was expressed at discrete puncta (Fig. 1). In cells grown as monolayers, the puncta had the typical morphology and distribution of focal adhesions observed in previous studies of VinTS in cultured adherent cells [25]. The colocalization of VinTS with paxillin (Fig. 6(a-c),(g)) is also consistent with the formation of focal adhesions at the VinTS sites observed in CHO-K1 monolayers. Paxillin is recruited to the integrin signaling layer of focal adhesions [39,40] and possesses a binding site (LD Motif) capable of binding the C-terminal (tail) of vinculin [41]. In contrast, the puncta in the 3D multicellular aggregates had varying shapes and their distribution appeared less regular. Using immunofluorescence, the presence of vinculin was confirmed at the VinTS puncta within 3D multicellular aggregates. However, the VinTS puncta in the 3D aggregates did not coincide with the presence of paxillin (Fig. 6(d-f),(h)). This suggests that the puncta containing VinTS in 3D aggregates differ from the focal adhesions found in the 2D monolayers. One hypothesis is that VinTS is primarily expressed at cadherin-mediated adherens junctions in the 3D multicellular aggregates. Nonetheless additional studies are required to support this possibility. The presence of vinculin antibody at the VinTS sites in Fig. 1 may be consistent with co-localization of VinTS with endogenous vinculin, or direct labeling of vinculin within VinTS. In either case, positive vinculin staining at the VinTS sites supported further investigation of vinculin tension at these sites in the 2D and 3D cultures.

Fluorescence lifetime measurements show that in both 2D and 3D cultures, the lifetime of VinTS is longer than the lifetime of VinTL (Fig. 3). This result is consistent with the properties of VinTS and VinTL. VinTS may be under tension via the binding of its head domain with talin and tail domain with F-actin [25]. Tension across VinTS decreases FRET between the donor (mTFP1) and acceptor (mVenus) and results in a longer lifetime. In addition, variations in the forces transmitted within the cell result in a broad range of lifetimes measured for VinTS. VinTL, on the other hand, is present at cell adhesions but remains unloaded due to the absence of the F-actin binding tail [25]. Consistent with this, VinTL measurements exhibited a shorter lifetime with less variance (Fig. 3). Furthermore, the lifetime of VinTS decreased after treatment with the Rho-associated kinase inhibitor Y-27637, while the lifetime of VinTL remained unchanged after treatment (Fig. 4). Taken together these results demonstrate that VinTS is under tension in both 2D and 3D culture conditions.

The measured lifetime was converted to FRET efficiency using a calibration technique previously developed to convert Apparent FRET efficiency, based on phase lifetime, to True FRET efficiency [35,38]. The FRET efficiency of VinTS measured here in CHO-K1 cells in 2D monolayers is 20.07%, which is comparable to the 18.07% FRET efficiency of VinTS measured in monolayers of iBMK cells using the same FLIM instrument [35]. However, both of these values are lower than the 25.1% FRET efficiency of VinTS we previously measured using the sensitized emission method in monolayers of CHO-K1 cells plated on Poly-D-lysine-coated coverslips or the 23.7% measured on fibronectin-coated coverslips [37]. VinTL FRET efficiency, which is 25.1% in the present study, is also lower than the 31.9% VinTL FRET measured in monolayers of CHO-K1 cells using the sensitized emission method [37]. A more pertinent comparison may be to consider the difference (absolute difference) between VinTS and VinTL FRET efficiency. In this FLIM-FRET study, this difference is 5% for the CHO-K1 monolayers cultured on plastic dishes and is comparable to a 6.6% difference measured using the sensitized emission method in CHO-K1 cells plated on Poly-D-lysine coated glass coverslips, but lower than the 8.2% difference measured in CHO-K1 cells plated on fibronectin-coated glass coverslips. While the lower VinTL FRET efficiency measured on the FLIM system compared with the sensitized emission method may be attributed to experimental or calibration differences, the FRET efficiency difference between VinTL and VinTS may be additionally affected by the cell's attachment to the different substrates.

In the 3D multicellular aggregates, the absolute FRET efficiency difference between VinTS and VinTL was 5.87%. Statistical analysis of the data by two-way ANOVA provide evidence that the interaction between plasmid condition (VinTS vs. VinTL) and culture condition (2D vs. 3D) was not significant ($p = 0.36$, Table 5). However, the FRET efficiency of both VinTS and VinTL was significantly lower in the 3D cultures compared with the 2D monolayers ($p < 0.001$, Table 5). This lower FRET efficiency could not be accounted for by photobleaching or calibration error. The FRET efficiency of mTFP1 remained unchanged in both culture conditions, demonstrating that the phase offset calibration of the FLIM system was not affected by the culture condition. In addition, while acceptor photobleaching was observed when measuring TSMod lifetime in the 2D monolayers, this had the effect of increasing the lifetime in the 2D monolayers compared with the 3D samples (Supplement 1). As such, a lower FRET efficiency (and longer lifetime) of VinTL and VinTS in the 3D cultures could not be explained by acceptor photobleaching in the 2D monolayers. Another potential explanation for the lower FRET efficiency of VinTS and VinTL in the 3D cultures could be the local environment present within the adhesions and the potential presence of distinct types of adhesions containing VinTS in the two types of cultures. This hypothesis is partially supported by the immunofluorescence data showing co-localization of paxillin at the sites of VinTS expression in the 2D monolayers but different spatial distribution of paxillin and VinTS in the 3D multicellular aggregates (Fig. 6). This may be due to a predominance of cadherin-mediated cell-cell contacts in the 3D aggregates that do not contain paxillin, while the presence of paxillin in the 3D aggregates without VinTS may reflect the presence of nascent focal adhesions to which vinculin was not recruited. Differences in FRET efficiency between the 2D monolayers and the 3D multicellular aggregates may be due to reported differences in cell-cell and cell matrix-interactions owing to changes in adhesion protein expression [42–45]. Changes in cell-cell and cell-matrix interactions, in turn, can influence the synthesis of different ECM components, which give rise to different mechanical properties such as changes in matrix stiffness [8]. Conversely, differences in ECM composition in 2D monolayers compared with 3D aggregates can affect cellular behaviors including the formation of stress fibers, migration and proliferation [8,46–48], which can further affect cell adhesions.

Our study demonstrates how 2D vs. 3D culture conditions utilized with the same cells can give rise to different outcomes. However, it is not clear whether the specific differences we observed between 2D and 3D cultures will be replicated in other cell types, or whether new differences will be found. Different types of adhesions predominate in 3D spheroids formed by different cell types [42–45] that could directly affect measurements of FRET efficiency such as those presented here. Thus, a priori, not all types of multicellular spheroids are necessarily the same. Nonetheless, the methods presented in our work may themselves be extended to other cell types and provide a way to probe these differences. Our results suggest that VinTL's FRET efficiency is sensitive to alterations in the adhesion environment around vinculin, while the difference between VinTS and VinTL FRET efficiency reports on whether vinculin is under tension. The ability to probe vinculin's environment and vinculin tension in different contexts can provide insight about the status of cell-mediated adhesions and the forces affecting a variety of fundamental cellular dynamics within living tissues. In two-dimensional cellular monolayers, actomyosin contractility and vinculin tension are involved in the assembly of focal adhesions, the establishment of cell polarity, the control of cell migration, and YAP translocation to the nucleus [49–53]. In 3D collagen matrices, vinculin tension promotes matrix degradation, cell polarity and cell migration [54–56], while decreased vinculin expression decreases FAK activation and accumulation at focal adhesions in 3D collagen cultures but not on 2D substrates [55]. Vinculin tension measured in vivo can report on cortical force oscillations contributing to the development of the murine mandibular arch [57]. Vinculin may even contribute to cancer cell resistance to chemotherapeutic treatment [58].

In summary, this study presents a side-by-side comparison of vinculin tension in 2D monolayers and 3D multicellular aggregate cultures from the same cell line. The results show that VinTS is under tension in both 2D and 3D cultures and therefore provide evidence that VinTS is present at adhesion sites within the 3D multicellular aggregates. However, preliminary evidence suggests that these adhesion sites may differ in composition from the typical focal adhesions observed in cells cultured in 2D monolayers on flat substrates. Further research is necessary to fully characterize the specific types of adhesions that form within the 3D multicellular aggregates and the properties of their environment that may influence the FRET efficiency measurements. We also note here that the 3D volumes were analyzed slice-by-slice in this study. Direct volumetric analysis in 3D by considering the mean lifetimes of 3D puncta, such as the ones depicted in Supplement 1, may be more appropriate in the future and might also result in slightly different mean values. A limitation of this study is the inefficiency of transfection and of labeling the cells within the aggregates coupled with limited optical imaging depth, thus restricting the data primarily to cells at the periphery of the 3D multicellular aggregates. In future work, VinTS expression could be increased using viral transduction. However, optical imaging may remain limited to a thickness a few cells deep at the edge of the multicellular aggregates. Still, investigation of cell attachment at the edge of tumor spheroids remains relevant in future studies aimed at applying the methods developed here to study the migration behavior of cells at the periphery of 3D aggregates.

Funding. National Science Foundation (CMMI-1825433); National Institutes of Health (R01 CA207725, R01 CA233188).

Acknowledgments. We thank James Y. Jiang for building the FLIM setup. We thank Brenton D. Hoffman (Duke University) for the mTFP1 plasmid and Marina A. Ayad for assistance with plasmid purification. This project was partially supported by NSF award CMMI-1825433 to NNB and NIH R01 CA207725 and CA233188 to MB.

Disclosures. The authors declare no conflicts of interest.

Data availability. Data underlying the results presented in this paper are not publicly available at this time but may be obtained from the authors upon reasonable request.

Supplemental document. See Supplement 1 for supporting content.

References

1. M. R. Zanotelli and C. A. Reinhart-King, "Mechanical Forces in Tumor Angiogenesis," in *Biomechanics in Oncology*, C. Dong, N. Zahir, and K. Konstantopoulos, eds. (2018), pp. 91–112.
2. C. C. DuFort, M. J. Paszek, and V. M. Weaver, "Balancing forces: architectural control of mechanotransduction," Nat. Rev. Mol. Cell Biol. **12**(5), 308–319 (2011).
3. D. A. Fletcher and D. Mullins, "Cell mechanics and the cytoskeleton," Nature **463**(7280), 485–492 (2010).
4. K. Franze, P. A. Janmey, and J. Guck, "Mechanics in neuronal development and repair," Annu. Rev. Biomed. Eng. **15**(1), 227–251 (2013).
5. M. A. Wozniak and C. S. Chen, "Mechanotransduction in development: a growing role for contractility," Nat. Rev. Mol. Cell Biol. **10**(1), 34–43 (2009).
6. C. T. Mierke, "The matrix environmental and cell mechanical properties regulate cell migration and contribute to the invasive phenotype of cancer cells," Rep. Prog. Phys. **82**(6), 064602 (2019).
7. B. M. Baker and C. S. Chen, "Deconstructing the third dimension - how 3D culture microenvironments alter cellular cues," Journal of Cell Science **125**, 3015–3024 (2012).
8. A. Saraswathibhatla, D. Indana, and O. Chaudhuri, "Cell-extracellular matrix mechanotransduction in 3D," Nat. Rev. Mol. Cell Biol. **24**(7), 495–516 (2023).

9. W. Muellerklieser, "Multicellular spheroids - a review on cellular aggregates in cancer-research," J Cancer Res Clin Oncol **113**(2), 101–122 (1987).
10. E. C. Costa, A. F. Moreira, D. de Melo-Diogo, *et al.*, "3D tumor spheroids: an overview on the tools and techniques used for their analysis," Biotechnol. Adv. **34**(8), 1427–1441 (2016).
11. A. S. Nunes, A. S. Barros, E. C. Costa, *et al.*, "3D tumor spheroids as in vitro models to mimic in vivo human solid tumors resistance to therapeutic drugs," Biotechnol. Bioeng. **116**(1), 206–226 (2019).
12. L. B. Weiswald, D. Bellet, and V. Dangles-Marie, "Spherical Cancer Models in Tumor Biology," Neoplasia **17**(1), 1–15 (2015).
13. S. J. Han, S. Kwon, and K. S. Kim, "Challenges of applying multicellular tumor spheroids in preclinical phase," Cancer Cell Int **21**(1), 152 (2021).
14. C. L. Roberge, D. M. Kingsley, D. E. Faulkner, *et al.*, "Non-Destructive Tumor Aggregate Morphology and Viability Quantification at Cellular Resolution, During Development and in Response to Drug," Acta Biomater. **117**, 322–334 (2020).
15. J. Barra, I. Crosbourne, C. L. Roberge, *et al.*, "DMT1-dependent endosome-mitochondria interactions regulate mitochondrial iron translocation and metastatic outgrowth," Oncogene **43**(9), 650–667 (2024).
16. M. S. Yousafzai and J. A. Hammer, "Using biosensors to study organoids, spheroids and organs-on-a-chip: a mechanobiology perspective," Biosensors **13**(10), 905 (2023).
17. G. Helmlinger, P. A. Netti, H. C. Lichtenbeld, *et al.*, "Solid stress inhibits the growth of multicellular tumor spheroids," Nat. Biotechnol. **15**(8), 778–783 (1997).
18. G. Cheng, J. Tse, R. K. Jain, *et al.*, "Micro-environmental mechanical stress controls tumor spheroid size and morphology by suppressing proliferation and inducing apoptosis in cancer cells," PLoS One **4**(2), e4632 (2009).
19. K. J. Curtis, J. Schiavi, M. J. Mc Garrigle, *et al.*, "Mechanical stimuli and matrix properties modulate cancer spheroid growth in three-dimensional gelatin culture," Journal of the Royal Society Interface **17**(173), 20200568 (2020).
20. M. Pandey, Y. J. Suh, M. Kim, *et al.*, "Mechanical compression regulates tumor spheroid invasion into a 3D collagen matrix," Phys. Biol. **21**(3), 036003 (2024).
21. A. S. Piotrowski-Daspit, J. Tien, and C. M. Nelson, "Interstitial fluid pressure regulates collective invasion in engineered human breast tumors via Snail, vimentin, and E-cadherin," Integrative Biology **8**(3), 319–331 (2016).
22. M. E. Dolega, M. Delarue, F. Ingremeau, *et al.*, "Cell-like pressure sensors reveal increase of mechanical stress towards the core of multicellular spheroids under compression," Nat. Commun. **8**(1), 14056 (2017).
23. L. Aoun, S. Larnier, P. Weiss, *et al.*, "Measure and characterization of the forces exerted by growing multicellular spheroids using microdevice arrays," Plos One **14**(5), e0217227 (2019).
24. C. T. Lee, E. L. Gill, W. Y. Wang, *et al.*, "Guided assembly of cancer ellipsoid on suspended hydrogel microfibers estimates multi-cellular traction force," Phys. Biol. **18**(3), 036001 (2021).
25. C. Grashoff, B. D. Hoffman, M. D. Brenner, *et al.*, "Measuring mechanical tension across vinculin reveals regulation of focal adhesion dynamics," Nature **466**(7303), 263–266 (2010).
26. F. Meng, T. M. Suchyna, and F. Sachs, "A fluorescence energy transfer-based mechanical stress sensor for specific proteins in situ," FEBS J. **275**(12), 3072–3087 (2008).
27. N. Borghi, M. Sorokina, O. G. Shcherbakova, *et al.*, "E-cadherin is under constitutive actomyosin-generated tension that is increased at cell-cell contacts upon externally applied stretch," Proc. Natl. Acad. Sci. U.S.A. **109**(31), 12568–12573 (2012).
28. D. E. Conway, M. T. Breckenridge, E. Hinde, *et al.*, "Fluid shear stress on endothelial cells modulates mechanical tension across VE-Cadherin and PECAM-1," Curr. Biol. **23**(11), 1024–1030 (2013).
29. B. R. Acharya, S. K. Wu, Z. Z. Lieu, *et al.*, "Mammalian diaphanous 1 mediates a pathway for E-cadherin to stabilize epithelial barriers through junctional contractility," Cell Rep. **18**(12), 2854–2867 (2017).
30. A. Kumar, M. Ouyang, K. Van Den Dries, *et al.*, "Talin tension sensor reveals novel features of focal adhesion force transmission and mechanosensitivity," Journal of Cell Biology **213**(3), 371–383 (2016).
31. M. Morimatsu, A. H. Mekhdjian, A. S. Adhikari, *et al.*, "Molecular tension sensors report forces generated by single integrin molecules in living cells," Nano Lett. **13**(9), 3985–3989 (2013).
32. B. E. Danielsson, B. G. Abraham, E. Mäntylä, *et al.*, "Nuclear lamina strain states revealed by intermolecular force biosensor," Nat. Commun. **14**(1), 3867 (2023).
33. L. S. Fischer, S. Rangarajan, T. Sadhanasatish, *et al.*, "Molecular force measurement with tension sensors," in *Annual Review of Biophysics*, Vol 50, 2021, K. A. Dill, ed. (2021), pp. 595–616.
34. T. R. Ham, K. L. Collins, and B. D. Hoffman, "Molecular tension sensors: moving beyond force," Curr. Opin. Biomed. Eng. **12**, 83–94 (2019).
35. J. P. Dumas, J. Y. Jiang, E. M. Gates, *et al.*, "FRET efficiency measurement in a molecular tension probe with a low-cost frequency-domain fluorescence lifetime imaging microscope," J. Biomed. Opt. **24**(12), Article Number: 1 (2019).
36. J. Schindelin, I. Arganda-Carreras, E. Frise, *et al.*, "Fiji: an open-source platform for biological-image analysis," Nature Methods **9**(7), 676–682 (2012).
37. C. Dubois, L. Houel-Renault, M. Erard, *et al.*, "Förster resonance energy transfer efficiency measurements on vinculin tension sensors at focal adhesions using a simple and cost-effective setup," J. Biomed. Opt. **28**(08), 082808 (2023).
38. D. Sumetsky, J. Y. Jiang, M. A. Ayad, *et al.*, "Linear behavior of the phase lifetime in frequency-domain fluorescence lifetime imaging of FRET constructs," Front. Phys. **9**, Article Number 648016 (2021).

39. P. Kanchanawong and D. A. Calderwood, "Organization, dynamics and mechanoregulation of integrin-mediated cell-ECM adhesions," Nat. Rev. Mol. Cell Biol. **24**(2), 142–161 (2023).
40. P. Kanchanawong, G. Shtengel, A. M. Pasapera, *et al.*, "Nanoscale architecture of integrin-based cell adhesions," Nature **468**(7323), 580–584 (2010).
41. M. C. Brown, J. A. Perrotta, and C. E. Turner, "Identification of LIM3 as the principal determinant of paxillin focal adhesion localization and characterization of a novel motif on paxillin directing vinculin and focal adhesion kinase binding," Journal of Cell Biology **135**(4), 1109–1123 (1996).
42. A. Ivascu and M. Kubbies, "Diversity of cell-mediated adhesions in breast cancer spheroids," International Journal of Oncology **31**, 1403–1413 (2007).
43. G. Rainaldi, A. Calcabrini, G. Arancia, *et al.*, "Differential expression of adhesion molecules (CD44, ICAM-1 and LFA-3) in cancer cells crown in monolayer or as multicellular spheroids," Anticancer Research **19**, 1769–1778 (1999).
44. B. Kim, N. R. Im, T. D. Yang, *et al.*, "Enhancement of aberrantly modified integrin-mediated cell motility in multicellular tumor spheroids," International Journal of Oncology **56**, 1480–1489 (2020).
45. E. Svirshchevskaya, E. Doronina, M. Grechikhina, *et al.*, "Characteristics of multicellular tumor spheroids formed by pancreatic cells expressing different adhesion molecules," Life Sci. **219**, 343–352 (2019).
46. J. Solon, I. Levental, K. Sengupta, *et al.*, "Fibroblast adaptation and stiffness matching to soft elastic substrates," Biophys. J. **93**(12), 4453–4461 (2007).
47. A. J. McKenzie, S. R. Hicks, K. V. Svec, *et al.*, "The mechanical microenvironment regulates ovarian cancer cell morphology, migration, and spheroid disaggregation," Sci. Rep. **8**(1), 7228 (2018).
48. I. Jahin, T. Phillips, S. Marcotti, *et al.*, "Extracellular matrix stiffness activates mechanosensitive signals but limits breast cancer cell spheroid proliferation and invasion," Front. Cell Dev. Biol. **11**, 1292775 (2023).
49. A. Carisey, R. Tsang, A. M. Greiner, *et al.*, "Vinculin regulates the recruitment and release of core focal adhesion proteins in a force-dependent manner," Curr. Biol. **23**(4), 271–281 (2013).
50. F. J. Li, A. Chen, A. Reeser, *et al.*, "Vinculin force sensor detects tumor-osteocyte interactions," Sci. Rep. **9**(1), 5615 (2019).
51. M. P. Ramirez, M. J. M. Anderson, M. D. Kelly, *et al.*, "Dystrophin missense mutations alter focal adhesion tension and mechanotransduction," Proc. Natl. Acad. Sci. U.S.A. **119**(25), e2205536119 (2022).
52. T. C. Shoyer, E. M. Gates, J. I. Cabe, *et al.*, "Coupling during collective cell migration is controlled by a vinculin mechanochemical switch," Proc. Natl. Acad. Sci. U.S.A. **120**(50), e2316456120 (2023).
53. E. N. Holland, M. A. Fernández-Yagüe, D. W. Zhou, *et al.*, "FAK, vinculin, and talin control mechanosensitive YAP nuclear localization," Biomaterials **308**, 122542 (2024).
54. C. T. Mierke, P. Kollmannsberger, D. P. Zitterbart, *et al.*, "Vinculin facilitates cell invasion into three-dimensional collagen matrices," Journal of Biological Chemistry **285**(17), 13121–13130 (2010).
55. A. Rahman, S. P. Carey, C. M. Kraning-Rush, *et al.*, "Vinculin regulates directionality and cell polarity in two- and three-dimensional matrix and three-dimensional microtrack migration," Molecular Biology of the Cell **27**(9), 1431–1441 (2016).
56. I. Thievessen, N. Fakhri, J. Steinwachs, *et al.*, "Vinculin is required for cell polarization, migration, and extracellular matrix remodeling in 3D collagen," Faseb Journal **29**(11), 4555–4567 (2015).
57. H. Tao, M. Zhu, K. Lau, *et al.*, "Oscillatory cortical forces promote three dimensional cell intercalations that shape the murine mandibular arch," Nat. Commun **10**(1), 1703 (2019).
58. A. C. Castro-Guijarro, A. M. Sanchez, M. I. Flamini, *et al.*, "Potential biomarkers associated with prognosis and trastuzumab response in HER2 + breast cancer," Cancers **15**(17), 4374 (2023).